Nanoscale

PAPER

View Article Online
View Journal | View Issue

Cite this: *Nanoscale*, 2024, **16**, 21048

Crafting "brick–mud" segregated nanocomposites: a novel approach to superior electromagnetic interference shielding, electrical insulation, and thermal conductivity in biopolymers†

Tong Liu,‡[a] Huiyao Feng,‡[a] Linbing Deng,‡[a] Chenhong Jin,[a] Henri Vahabi,[b] Mohammad Reza Saeb[c] and Tairong Kuang*[a]

Received 1st August 2024,
Accepted 12th October 2024

DOI: 10.1039/d4nr03175j

rsc.li/nanoscale

As electronic devices continue to be integrated, miniaturized, and operated at higher frequencies, the demand for green, advanced polymer nanocomposites with superior electromagnetic interference (EMI) shielding, thermal conduction, and electrical insulation properties significantly increases. However, achieving such multifunctional nanocomposites is challenging due to the inherent contradiction between electrical and magnetic properties. Biopolymer nanocomposites of polycaprolactone (PCL)/boron nitride (BN)@polylactic acid (PLA)/multi-walled carbon nanotubes (CNTs) ((PCL/BN)@(PLA/CNTs)) exhibit a unique "brick–mud" segregated double-network structure. This configuration effectively separates high-melting-point PLA/CNTs conductive phase from the PCL/BN insulating matrix. PLA/CNTs particles contribute to enhanced EMI shielding by attenuating electromagnetic waves, while also improving insulation by disrupting electron transfer within the PCL/BN phase. Additionally, incorporating conductive CNTs and thermal conductive BN further boosts the thermal conductivity (TC) of the nanocomposites. The structured sample (s-8B8C), which contains 8 wt% BN and 8 wt% CNTs, achieves an EMI shielding effectiveness (SE) of 31.4 dB in the X-band, a TC of 0.6 W m^{-1} K^{-1}, and a volume resistivity of 7.2 × 10^{11} Ω cm. In summary, the "brick–mud" segregated structure facilitates the development of advanced biopolymer nanocomposites for electronic applications, leveraging sustainable materials for broad potential use.

Introduction

The increasing complexity of electronic components in electronic devices highlights the urgent need for substrates that excel in both thermal management and electromagnetic interference (EMI) shielding. These attributes are crucial not only to enhance device performance but also to ensure their durability and reliability in clinical environments. Typically, EMI shielding effectiveness (SE) is directly linked to the material's electrical conductivity, with substrates exhibiting higher conductivity often providing better shielding capabilities.[1,2] However, conventional metals, despite their excellent thermal conductivity (TC), often fail to meet the requirements for applications that demand stringent electrical insulation. This limitation is exacerbated by concerns over their excessive electrical conductivity, cost, and easy corrosion, posing significant challenges in developing electronic devices where safety and durability are essential.[3–5]

Recently, polymer nanocomposites have garnered attention due to their satisfactory TC and EMI shielding, alongside economic and processing benefits.[6–12] Yet, achieving an optimal balance among electrical insulation, thermal conduction, and EMI shielding in these materials remains a considerable challenge. Traditional approaches often employ a layered assembly of insulative and conductive layers. For instance, Zhan *et al.*[13] successfully achieved uniform dispersion of carbon nanotubes (CNTs) and hexagonal boron nitride (h-BN) within natural rubber by employing the solution blending method, followed by the preparation of multilayer nanocomposites through layer-by-layer filtration. These nanocomposites exhibited a TC of 0.25 W m^{-1} K^{-1} and an EMI SE of 22.4 dB. Remarkably, they maintained effective vertical insulation with 8 wt% CNTs and 12 wt% h-BN, respectively. Liu *et al.*[14] uniformly incorporated BN and titanium carbide (MXene) into polydimethylsiloxane

[a]*Functional Polymers & Advanced Materials (FPAM) Lab, Zhejiang Key Laboratory of Plastic Modification and Processing Technology, College of Materials Science and Engineering, Zhejiang University of Technology, Hangzhou 310014, China. E-mail: kuangtr@zjut.edu.cn*

[b]*Université de Lorraine, CentraleSupélec, LMOPS, Metz, France*

[c]*Department of Pharmaceutical Chemistry, Medical University of Gdańsk, J. Hallera 107, 80-416 Gdańsk, Poland*

†Electronic supplementary information (ESI) available. See DOI: https://doi.org/10.1039/d4nr03175j

‡These authors contributed equally to the work.

(PDMS) using ultrasonication and stirring, producing multilayer composite films by sequential coating and curing. The performance of an 11-layer MXene/BN/PDMS composite was notable, with a TC of 0.65 W m^{-1} K^{-1}, an EMI SE exceeding 30 dB, and a volume resistivity of 2.9×10^{12} Ω cm. However, these multilayer structures exhibit anisotropy, limiting insulation to the vertical plane and permitting high conductivity horizontally. This suggests that multilayer configurations may not be universally suitable for comprehensive thermal management in electronic components.

To address these challenges, a novel segregated structural design has been developed.[15,16] The composite material is fabricated *via* hot-pressing conductive polymer composite particles uniformly coated with an insulating, thermally conductive filler. This approach aims to improve TC while maintaining electrical insulation and providing effective EMI shielding, thereby optimizing the multifunctional performance of the material. For instance, Zhang *et al.*[17] utilized a water vapor-induced phase separation (WVIPS) method to prepare polyvinylidene difluoride (PVDF)@CNT microspheres. They then prepared PVDF@CNT/BN nanocomposites with a unique segregated double-network structure by mechanically mixing BN on the surface of the microspheres. The composite demonstrated a TC of 0.83 W m^{-1} K^{-1}, an electrical conductivity of 8.33×10^{-14} S cm^{-1}, and an EMI SE of 8.68 dB, with 5 wt% CNTs and 40 wt% BN. In this composite, the addition of insulating fillers such as BN is crucial for impeding electronic transmission and establishing a thermal conduction network. However, challenges persist, such as the risk of defects compromising processing performance with increased BN content.

In this work, an innovative approach was developed to overcome the inherent drawbacks of high electrical conductivity in the plane direction typical of multilayer structures. We present a polymer composite with a "brick–mud" segregated structure, and the schematic diagram for the preparation process is shown in Fig. 1. This novel concept involves uniformly dispersing high melting point polymer composite particles, the "bricks", within a low melting point polymer composite "mud", thereby conferring multiple functionalities to the nanocomposites. Specifically, this work uses multi-walled carbon nanotube (CNT)-embedded high melting point polylactic acid (PLA) composites as the "bricks" and an insulating boron nitride (BN) filler embedded within low-melting polycaprolactone (PCL) nanocomposites as the "mud". In the (PCL/BN)@(PLA/CNTs) nanocomposites, the PLA/CNTs provide EMI shielding, while the PCL/BN phases ensure insulation. Additionally, the interaction between BN and CNTs not only prevents the formation of conductive networks but also establishes efficient heat dissipation pathways. This work offers a novel strategy for developing next-generation biopolymer nanocomposites suitable for electronic equipment, emphasizing sustainability for broader applications.

Experimental

Materials

Polylactic acid (PLA, grade 4032D), provided by NatureWorks Co., Ltd (USA). It has a molecular weight of 1.85×10^5 g mol^{-1}, contains 2% D-lactic acid (D-LA), and has a density of 1.24 g cm^{-3}. Polycaprolactone (PCL, grade CAPA 6500) with a molecular weight of 5.00×10^4 g mol^{-1} and a density of 1.02 g cm^{-3} was supplied by Perstorp Ltd (Sweden). Multi-walled carbon nanotubes (NC-7000), featuring an average diameter of 9.5 nm and a length of 1.5 μm, were obtained from Nanocyl Co., Ltd (Belgium). Additionally, 99% pure boron nitride (BN) flakes

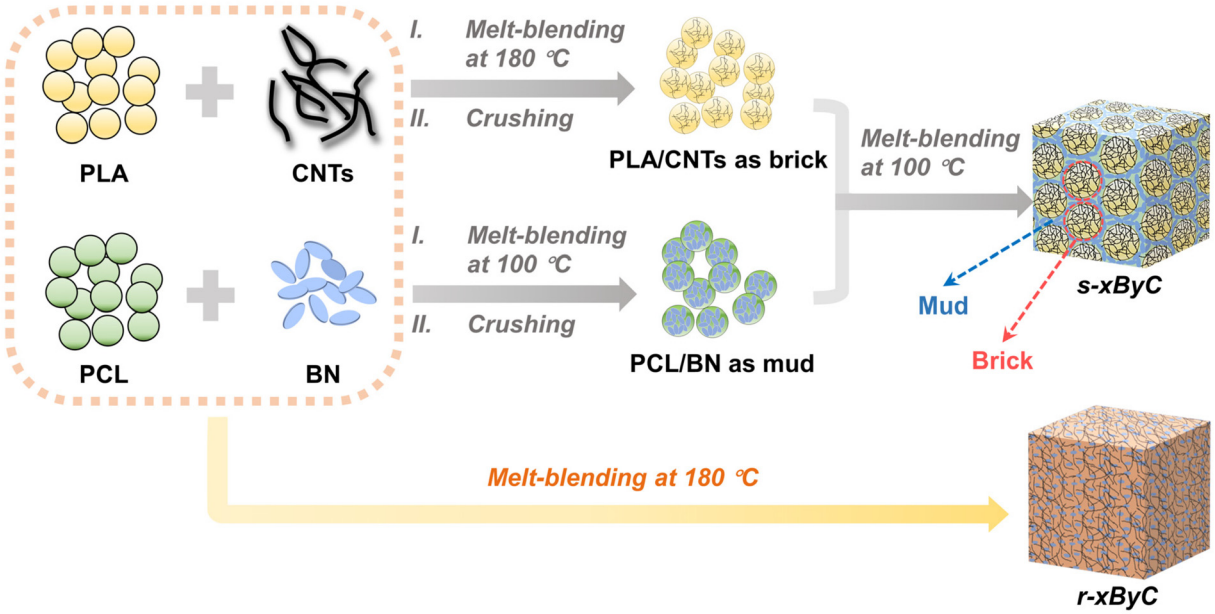

Fig. 1 Schematic representation of the preparation process of "brick–mud" segregated structured multifunctional nanocomposites.

with particle sizes ranging from 15 to 20 μm were sourced from Shandong Pengcheng Special Ceramics Co., Ltd (China).

Preparation of (PCL/BN)@(PLA/CNTs) composites with a "brick–mud" segregated structure

Initially, PLA, PCL, CNTs, and BN were dried separately in a blast oven at 70 °C, 50 °C, 100 °C, and 100 °C, respectively, for 12 h to remove moisture. Subsequently, PCL and BN were mixed at a specific ratio (20 wt% PCL to 40 wt% BN), melted, and uniformly blended using a torque rheometer to fabricate the PCL/BN composite. The mixing parameters were set at 100 °C temperature, 50 rpm rotor speed and a 5 min duration. In the final "brick–mud" segregated structure, the PCL/BN phase acts as the "mud". The PLA/CNTs composites, containing 5 wt% and 10 wt% CNTs, were prepared through melt-blending at 180 °C, 50 rpm, and for a duration of 5 min. The resulting PLA/CNTs particles were then mechanically crushed using a crusher (DFT-40, Wuxi Jiuping, China), and particles with sizes ranging from 100–500 μm were selected to serve as the "bricks" in the final "brick–mud" segregated structure. The PLA composites with 5 wt% and 10 wt% CNTs were designated PLA/5C and PLA/10C, respectively. To fabricate the final "brick–mud" segregated (PCL/BN)@(PLA/CNTs) composites, the "brick" and "mud" components were blended in a 20 : 80 mass ratio using a torque rheometer. The mixing parameters were set to 100 °C, 25 rpm rotor speed, and a 5 min duration. Conversely, composites with randomly dispersed fillers were also prepared using a torque rheometer under identical component ratios. For simplicity, the "brick–mud" and randomly dispersed composites were labeled as s-*x*B*y*C and r-*x*B*y*C, where "*x*" and "*y*" represent the mass fractions of BN and CNTs, respectively, in the final samples. Table 1 provides the detailed composition of each sample.

Characterization

Morphological characterization. The fracture surface morphology of the s-*x*B*y*C and r-*x*B*y*C composites was observed using a Digital Microscope (DM, DM4, China) and a scanning electron microscope (SEM, Regulus 8100, HITACHI). Brittle fracture surfaces were prepared by low-temperature treatment, with the samples cooled in liquid nitrogen for 2 h. Prior to SEM analysis, the fracture surfaces were coated with gold for 90 s under vacuum. The operating voltage for SEM was set to 10 kV.

Electrical conductivity. Electrical conductivity measurements for all samples were conducted in dry air at ambient temperature using a four-point probe resistivity system (RTS-9, Guangzhou Four Probes Technology Company Ltd, China) and a high-resistance meter (ZC36, Shanghai Anbiao Electronic Co., Ltd, China).

Thermal conductivity (TC). The thermal diffusion coefficient of the composite was determined using a Netzsch LFA 467 laser TC instrument (Germany). Test samples, 1 mm thick discs with a diameter of 12.7 mm, were assessed at 25 °C. Prior to testing, the sample surfaces were coated with carbon. TC was calculated using eqn (1):[10]

$$\lambda = \alpha \cdot C_p \cdot \rho \quad (1)$$

where α represents the thermal diffusion coefficient, C_p denotes the specific heat capacity, and ρ signifies the density of the sample.

C_p for each sample was measured by differential scanning calorimetry (DSC) at a heating rate of 10 °C min^{-1} from 10 °C to 40 °C under a nitrogen atmosphere. The density of each sample was determined using a JHY-S300 solid–liquid densitometer (Xiamen Jinheyuan Technology Co., Ltd, China), with results averaged from three measurements.

Electromagnetic interference (EMI) shielding performance. EMI shielding involves using materials to reflect or absorb electromagnetic wave energy, thereby attenuating high-energy electromagnetic wave penetration. The EMI shielding effectiveness (EMI SE) is quantified in decibels (dB) using eqn (2),[18] which assesses the ratio between the energy of incident (P_i) and transmitted (P_t) waves:

$$\mathrm{SE\ (dB)} = 10\log P_i/P_t \quad (2)$$

The EMI performance of the 3 mm-thick composites was evaluated within the X-band frequency range (8.2–12.4 GHz) using a vector network analyzer (Ceyear 3672C-S, Ceyear Technologies Co., Ltd, China).

Table 1 Components of nanocomposites with different structures

Sample	Full name	Structure	PLA (wt%)	CNTs (wt%)	PCL (wt%)	BN (wt%)
PLA/5C	PLA/5CNTs	Random	95	5	0	0
PLA/10C	PLA/10CNTs	Random	90	10	0	0
PCL/20B	PCL/20BN	Random	0	0	80	20
PCL/40B	PCL/40BN	Random	0	0	60	40
s-4B4C	20(PCL/20BN)@80(PLA/5CNTs)	Segregated	76	4	16	4
s-4B8C	20(PCL/20BN)@80(PLA/10CNTs)	Segregated	72	8	16	4
s-8B8C	20(PCL/40BN)@80(PLA/10CNTs)	Segregated	72	8	12	8
r-4B4C	16PCL/76PLA/4BN/4CNTs	Random	76	4	16	4
r-4B8C	16PCL/76PLA/4BN/8CNTs	Random	72	8	16	4
r-8B8C	16PCL/76PLA/8BN/8CNTs	Random	72	8	12	8

Results and discussion

Morphology of the (PCL/BN)@(PLA/CNTs) composites

To prepare composites with a "brick–mud" segregated structure, the PLA/CNTs composite particles obtained through melt blending were pulverized using liquid nitrogen, and particles with sizes ranging from 100 to 500 μm were selected as the "bricks". Fig. 2a and b show the SEM images and particle size distribution of the PLA/CNTs particles, respectively. According to statistics, most of the PLA/CNTs particles are distributed between 200 and 350 μm, with an average particle size of 305.7 μm. Subsequently, the selected PLA/CNTs particles were blended with PCL/BN composite particles at a temperature between the melting points of PLA and PCL. In this process, PCL/BN was in a flowable melt state (as "mud") and PLA/CNTs were in a solid state (as "bricks") (refer to Fig. S1† for DSC test results). Digital microscope (DM) was utilized to examine the cross-sectional morphology of s-8B8C composites, which exhibit a 'brick–mud' segregated structure, as shown in Fig. 2c. For the cross-sectional structure of other samples, see Fig. S2.† In these images, the white regions represent the PCL/BN insulating component, while the black parts represent the PLA/CNTs conducting component. The SEM images clearly show that the segregated black PLA/CNTs conductive particles are tightly wrapped by the continuous white PCL/BN insulating phase, preventing contact between the black particles and thus interrupting the conductive path. Owing to the significant melting point difference between PCL and PLA, the PLA/CNTs particles, acting as a "filler", remain solid and are uniformly dispersed in the PCL/BN melt at 100 °C. Consequently, the CNTs within the PLA/CNTs particles do not merge into the PCL/BN melt. This ensures that the CNTs do not enter into the PCL/BN melt, maintaining the excellent insulating properties of s-*x*B*y*C composites. Conversely, the DM photographs of the direct melt-mixed r-8B8C composites (Fig. 2d) reveal sporadic white dots on a continuous black substrate, indicating random dispersion of CNTs, which is less effective for achieving insulation. The dispersion of the filler within the matrix was analyzed, and the "brick–mud" segregated structure was compared to the random structure using SEM to examine the cross-sections of each composite. Fig. 3 displays a comparable 'brick–mud' segregated structure in the s-4B4C, s-4B8C, and s-8B8C

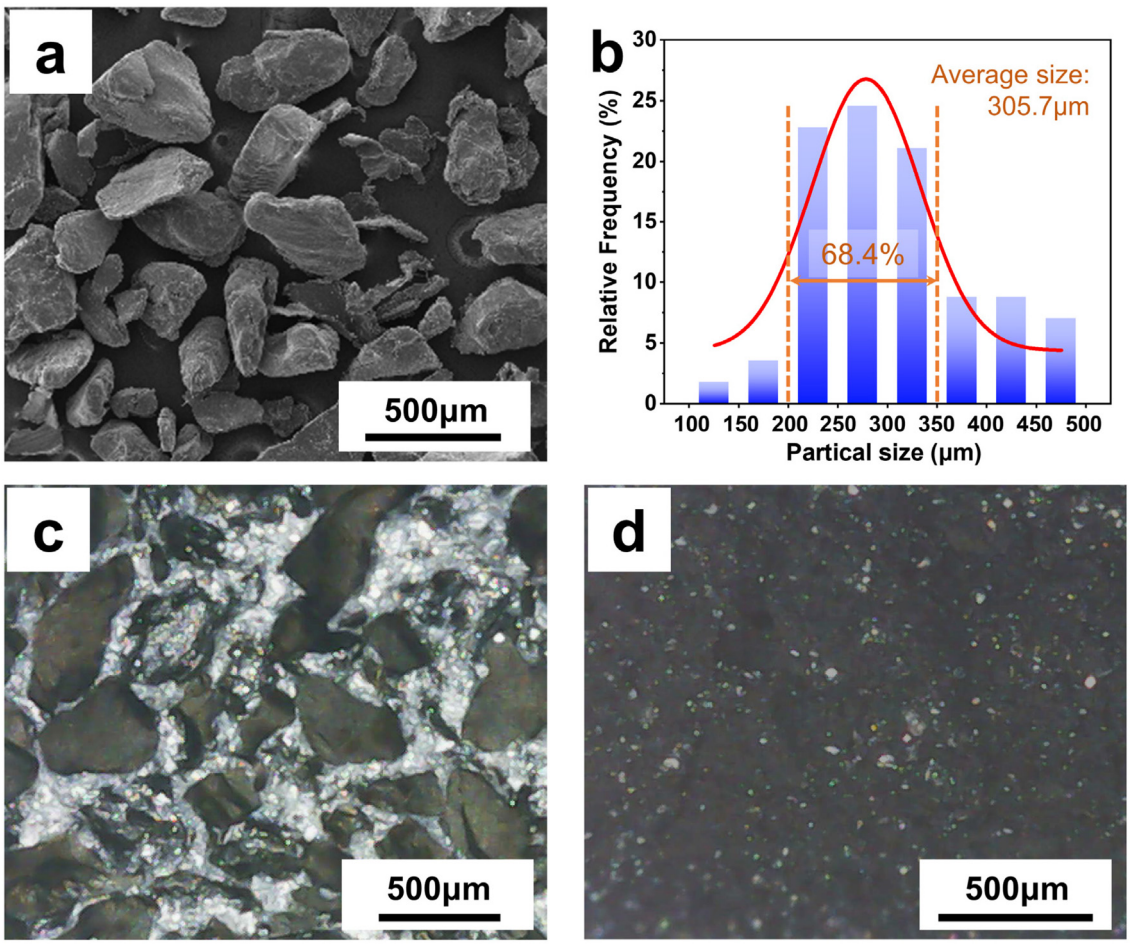

Fig. 2 (a) SEM image of size-sieved PLA/10C composite particles and (b) their corresponding size distribution statistics. DM images of cryo-fractured surfaces: (c) s-8B8C and (d) r-8B8C.

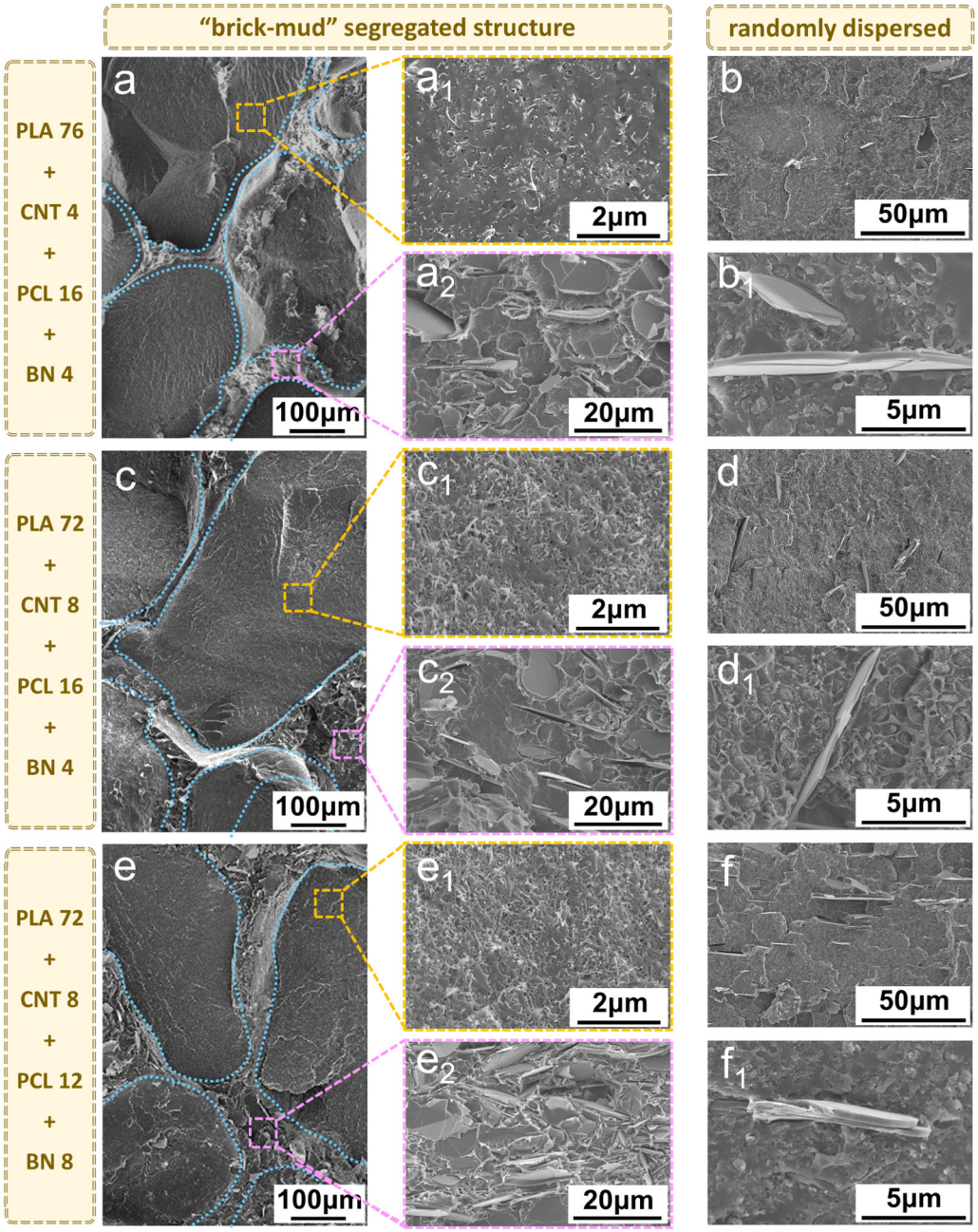

Fig. 3 SEM images of cryo-fractured surfaces of: (a) s-4B4C, (b) r-4B4C, (c) s-4B8C, (d) r-4B8C, (e) s-8B8C, and (f) r-8B8C.

combinatorial sites at a low magnification. The continuous 'mud' is composed of PCL/BN, while the dispersed phase is made up of PLA/CNTs particles acting as 'bricks'. Magnified views of the "brick" component (Fig. 3a_1, c_1 and e_1) show that both 5 wt% and 10 wt% CNTs fillings create a distinct overlap in the PLA matrix. However, in Fig. 3a_2 and c_2, some areas lack complete connection pathways at 20 wt% BN filling, potentially hindering the samples' TC improvement. With the BN content increased to 40 wt%, Fig. 3e_2 clearly shows numerous BN flakes in contact with each other. Increasing the filler concentration enhances the development of a robust and well-established conduction network. In particular, the conductive network formed by interconnected CNTs endows the PLA/CNTs "bricks" with excellent EMI shielding properties. The interconnection between BNs as well as between BNs and CNTs creates multiple low-resistance thermal conduction paths, enhancing the composites' TC. Surprisingly, r-*x*B*y*C composites, prepared through direct melt blending, exhibit a randomly dispersed filler, resulting in a microstructure distinctly different from that of s-*x*B*y*C. In r-*x*B*y*C composites, BN and CNTs are randomly dispersed throughout the polymer matrix, as opposed to forming segregated structures. The lack

of a segregated structure results in BN being dispersed uniformly throughout the polymer. This impedes selective aggregation and obstructs the development of rapid thermal conduction pathways. For instance, in Fig. 3f, although the BN content is 8 wt%, only a few BN nanoflakes are visible, unlike the dense BN network shown in Fig. 3e$_2$. In the r-8B8C sample, element B is uniformly and randomly distributed, while in the s-8B8C sample, element B is selectively aggregated. These phenomena are further confirmed by the EDS images in Fig. S6.† This effect is particularly evident at lower BN loadings (see Fig. 3b and 3d). Notably, the BN content in the PCL matrix of the s-8B8C composite is 20 wt% or 40 wt%, while in the r-8B8C composite's PLA/PCL matrix, it is only 4 wt% or 8 wt%. Additionally, in the randomly dispersed system, CNTs are uniformly dispersed throughout the polymer matrix and the dispersed BN does not block electron transport, which affects the electrical insulation properties of r-*x*B*y*C.

Electrical insulation properties

The electrical conductivity results of r-*x*B*y*C and s-*x*B*y*C composites and PLA/PCL blends are presented in Fig. 4 and Table S1.† Fig. 4a shows that the PLA/PCL blend, with a volume resistivity of 2.3 × 10^{15} Ω cm, is a typical electrically insulating material. However, in the r-*x*B*y*C composite without a segregated structure, the introduction of hybrid filler led to a rapid decrease in volume resistivity by approximately 15 orders of magnitude, falling below 2.4 Ω cm. Introducing conductive CNTs through direct melt blending converted the PLA/PCL blends from electrical insulators into effective conductors. As the CNTs content increased from 4 wt% to 8 wt%, the reduction in volume resistivity slowed, suggesting that 4 wt% CNTs are sufficient to form a relatively effective conductive network in r-*x*B*y*C composites. Fluctuations in the volume resistivity of r-*x*B*y*C composites were consistent with filler distri-

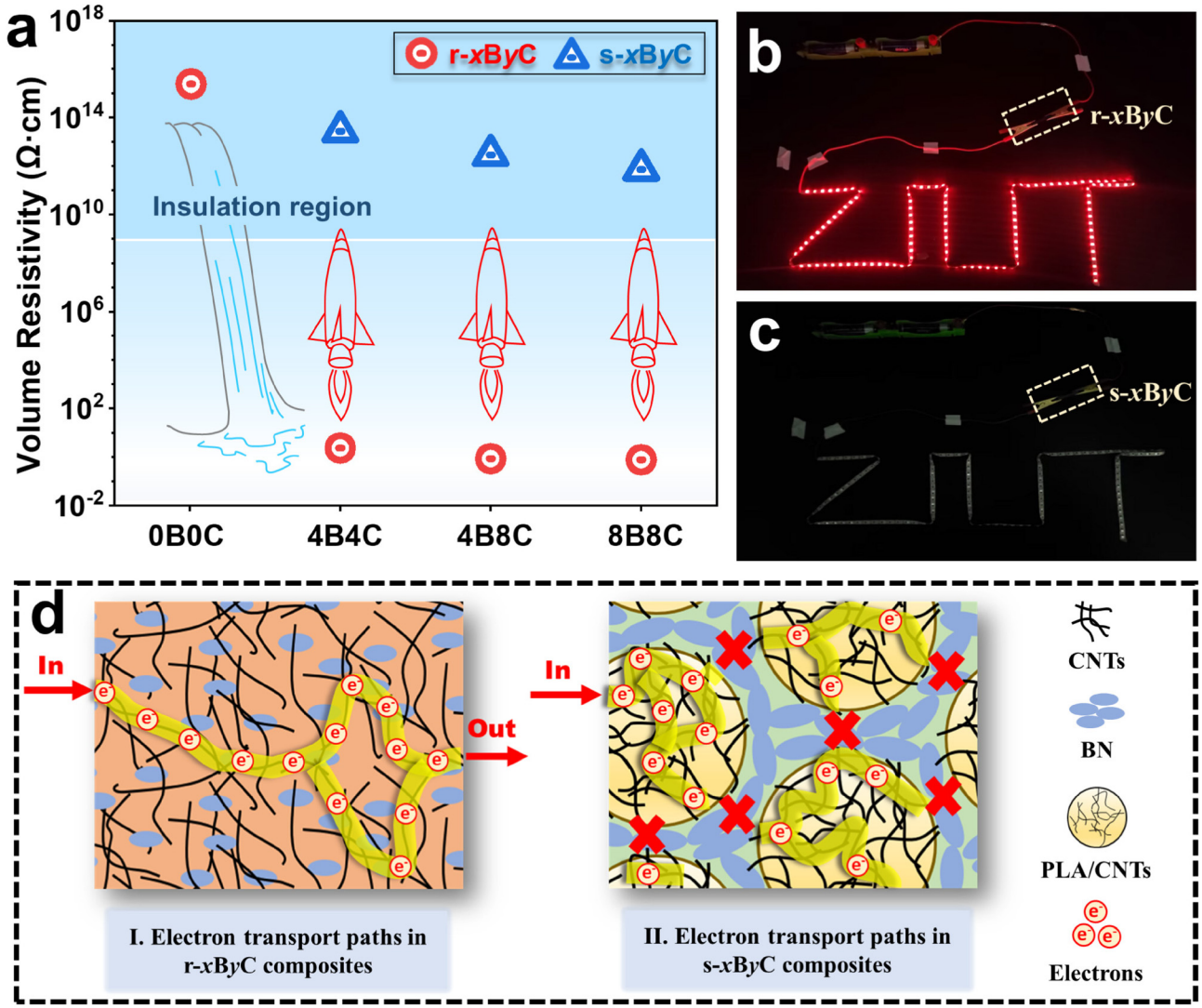

Fig. 4 Electrical properties of various nanocomposites: (a) volume resistivity, electrical conductivity verification test of (b) r-*x*B*y*C and (c) s-*x*B*y*C nanocomposites, and (d) schematic diagram of electron transport paths in r-*x*B*y*C and s-*x*B*y*C nanocomposites.

bution states observed by SEM (refer to Fig. 3). Interestingly, despite a decrease in the volume resistivity for s-*x*B*y*C composites with "brick–mud" segregated structures compared to those of PLA/PCL blends, all samples retained their insulating properties.[19,20] For instance, the volume resistivity of the s-4B4C sample remains high at 2.7×10^{13} Ω cm, approximately 2 orders of magnitude lower than that of the PLA/PCL blend and significantly higher than r-4B4C (2.4 Ω cm). Even with an increase in CNTs content to 8 wt%, the volume resistivities of the s-4B8C and s-8B8C remained high at 3.9×10^{12} Ω cm and 7.2×10^{11} Ω cm, respectively, keeping them in the insulating range. Further analysis shows that the volume resistivity of s-8B8C is marginally lower than that of s-4B8C. The observed phenomenon results from the reduced mobility within the PCL/BN composites with increasing BN content, which restricts the interaction among adjacent PLA/CNTs particles in s-*x*B*y*C "brick–mud" segregated structured composites.[21,22] Consequently, this study did not further increase the BN content, despite its apparent benefits for enhancing TC. Fig. 4b clearly shows the excellent electrical conductivity of r-*x*B*y*C composites, indicated by the bright red LEDs, while s-*x*B*y*C samples exhibit insulator characteristics, as shown in Fig. 4c. Furthermore, Fig. 4d demonstrates that within a randomly dispersed system, the superior electrical conductivity and high aspect ratio of CNTs contribute to the formation of a continuous conductive network, regardless of BN incorporation. Previous research, including PLA and PLA/CNTs composites (as shown in Fig. S3–S5†), has shown that conductive percolation in composites typically begins at low CNTs loadings, such as 2 wt% or less, resulting in a significant increase in conductivity.[23,24] Thus, r-*x*B*y*C composites exhibit excellent electrical conductivity. Conversely, in the s-*x*B*y*C composites with segregated structures, the PCL/BN "mud" acts as a barrier, limiting CNTs to forming conductive networks within individual PLA/CNTs particles and preventing cross-particle connectivity. Essentially, the insulating nature of PCL/BN disrupts the electron transport paths, enabling the s-*x*B*y*C composites to maintain excellent electrical insulation, as depicted in Fig. 4d. The electrical conductivity results clearly demonstrate that the "brick–mud" segregated structures in the composites effectively obstruct electron transport, thereby preserving the insulating properties.

EMI shielding performance

Fig. 5 presents the EMI SE test results for the composites. The PLA/PCL blend, due to the absence of conductive fillers, exhibit negligible electromagnetic wave shielding, yielding an EMI SE of merely 1.5 dB. Incorporating CNTs significantly enhances the EMI SE of the composites. As observed in Fig. 5a, all samples maintain relatively stable shielding effects within the X-band frequency range. The s-*x*B*y*C composites show slightly lower EMI SE compared to r-*x*B*y*C composites,

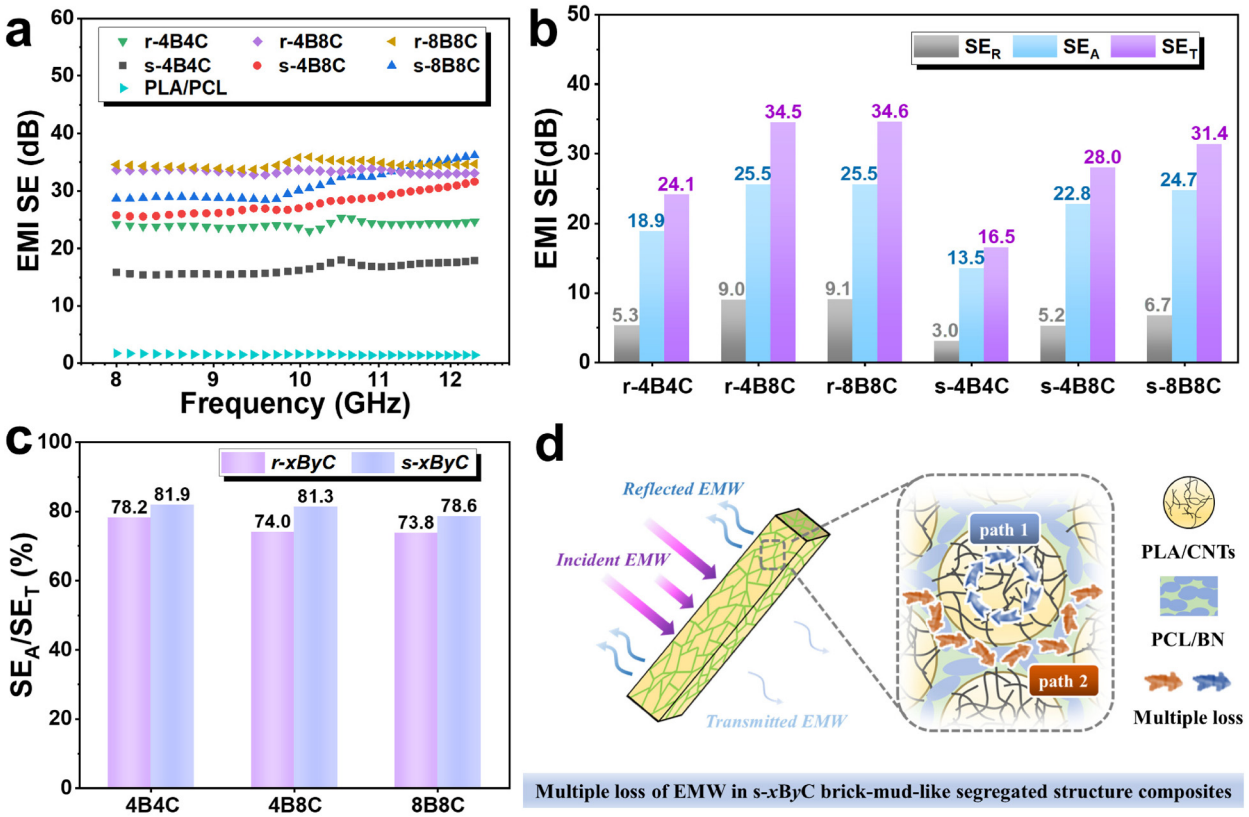

Fig. 5 EMI SE of X-band randomly distributed and "brick–mud" segregated structured nanocomposites: (a) EMI SE, (b) EMI SE_R, SE_A and SE_T, and (c) SE_A/SE_T and (d) schematic diagram of the shielding mechanism of "brick–mud" segregated structures against electromagnetic waves (EMW).

primarily due to the extensive conductive network present in the r-*x*B*y*C samples (please refer to the SEM images in Fig. 3 for further details). The EMI shielding performance in magnetic materials is generally driven by mechanisms such as magnetic resonance, eddy current loss, and polarization loss.[25,26] In contrast, for non-magnetic materials, high electrical conductivity is often considered crucial for achieving effective shielding.[27] Conductive materials primarily interact with incident electromagnetic waves through reflection losses, significantly contributing to EMI shielding.[28]

As a result, the s-*x*B*y*C composites, with their segregated structures, exhibit slightly lower EMI SE compared to r-*x*B*y*C composites due to the inherent electrical insulation properties of the segregated structure. In the s-*x*B*y*C composites, the conductive PLA/CNTs particles are encapsulated within the insulating PCL/BN composites, limiting the formation of continuous conductive pathways and reducing the ability to effectively reflect and absorb electromagnetic waves. Additionally, gaps between the segregated conductive particles in the s-*x*B*y*C composites may allow for some electromagnetic wave transmission, further contributing to the reduced shielding effectiveness. Despite this marginal reduction in EMI shielding performance, the s-*x*B*y*C composites maintain stable electrical insulation properties and still provide considerable shielding, making them suitable for practical applications where a balance between electrical insulation and EMI shielding is required. Furthermore, the r-*x*B*y*C composites achieve a total shielding effectiveness (SE_T) exceeding 20 dB, while the s-*x*B*y*C composites exhibit lower shielding performance at low CNTs contents. For example, the r-4B4C composite shows an EMI SE of 24.1 dB at lower CNTs contents, compared to 16.5 dB for the insulating s-4B4C composite. However, the difference in shielding effectiveness diminishes as the CNTs content increases to 8 wt%. The s-4B8C and s-8B8C composites reach EMI SE_T values of 28.0 dB and 31.4 dB, respectively, surpassing commercial standards. Increasing the CNTs content from 4 wt% to 8 wt% significantly improves the SE_A and SE_T in both structures. Conversely, increasing the BN content from 4 wt% to 8 wt% causes minimal changes in the SE_A and SE_T of the r-*x*B*y*C composites. However, the effect of the BN content in s-*x*B*y*C composites is more pronounced in the s-*x*B*y*C composites. A 4 wt% increase in BN content represents a 20 wt% increase in actual BN concentration within the PCL matrix. This significantly affects the fluidity of the PCL/BN "mud", allowing a limited number of adjacent PLA/CNTs "bricks" to establish contact. Consequently, the local electrical conductivity is enhanced, as reflected in the electrical conductivity test results presented in Fig. 4a. To explore differences in EMI shielding mechanisms between random and "brick–mud" segregated structures, the *A*, *R*, and *T* values are presented in Fig. S7.† Due to the presence of the highly conductive CNTs, both composite structures demonstrate a reflection-dominated shielding mechanism ($A < R$). However, the introduction of segregated structures in the s-*x*B*y*C composites leads to an increase in *A* value compared to the r-*x*B*y*C composites. Meanwhile, the SE_A/SE_T ratios for both composite types were calculated. As shown in Fig. 5c, the s-*x*B*y*C composites exhibit higher SE_A/SE_T ratios, varying between 78% and 82%, compared to 73%–79% for the r-*x*B*y*C composites of similar composition. The variations in *A*, *R*, *T*, and SE_A/SE_T values indicate that the "brick–mud" segregated structure of the s-*x*B*y*C composites contributes more to absorption loss in electromagnetic wave shielding.[29,30] For a clearer understanding of the absorption-dominant benefits of the "brick–mud" segregated structure, Fig. 5d presents a schematic of the EMI shielding mechanism within the s-*x*B*y*C composites. The high conductivity of PLA/CNTs particles leads to the attenuation of electromagnetic wave energy through reflection loss upon interaction with the s-*x*B*y*C composite surface. The wave entering the sample undergoes absorption through multiple reflections among conductive PLA/CNTs particles, with additional attenuation occurring within the particles themselves. Ultimately, most of the incident electromagnetic energy in the shielding material is converted into internal energy, with only a minimal amount propagating through the surrounding environment. The double absorption mechanism of the s-*x*B*y*C composite results in more pronounced absorption advantages compared to those observed in the r-*x*B*y*C composite.

Thermal conductivity (TC)

For polymer-based materials, phonon thermal conduction is the primary mechanism for TC, typically quantified as TC (W m^{-1} K^{-1}).[31] The TC results of the prepared composites are presented in Fig. 6 and detailed in Table S2.† As depicted in Fig. 6a, the TC of the pure PCL/PLA sample is only 0.15 W m^{-1} K^{-1}, which is attributed to the separation of lamellar crystals by irregular chain segments in the amorphous regions of the semi-crystalline polymers, hindering phonon transport and reducing TC.[32–34] Incorporating fillers, notably CNTs (2000–6000 W m^{-1} K^{-1}) and BN (400 W m^{-1} K^{-1}),[35,36] markedly improves the TC of the composites, due to their high intrinsic TC. In polymer-based composites, the widely accepted thermal conduction path theory suggests that heat transfer occurs along a continuous network of highly conductive fillers with low thermal resistance. The addition of a minimal amount of thermal conductive filler results in insufficient contact among particles, leading to negligible improvement in TC. Therefore, substantial TC enhancement is observed only when the filler concentration reaches a threshold sufficient for extensive contact, allowing heat to conduct rapidly along the low-resistance pathways.[32,37] At low concentrations, the TC of r-4B4C is comparable to or even slightly higher than that of the s-4B4C composite. This behavior is attributed to the insufficient BN content in the PCL/BN "mud" of the s-4B4C composite, as seen in Fig. $3a_2$ and c_2, which limits the formation of abundant thermal conduction pathways. In contrast, in the randomly dispersed r-4B4C samples, contact between BN and CNTs facilitates the formation of more effective thermal pathways.

However, the TC responds differently to the increasing filler content. Notably, the TC of the s-8B8C composite increased significantly to 0.60 W m^{-1} K^{-1}, compared to 0.42 W m^{-1} K^{-1} in the r-8B8C composite. This enhancement is primarily attrib-

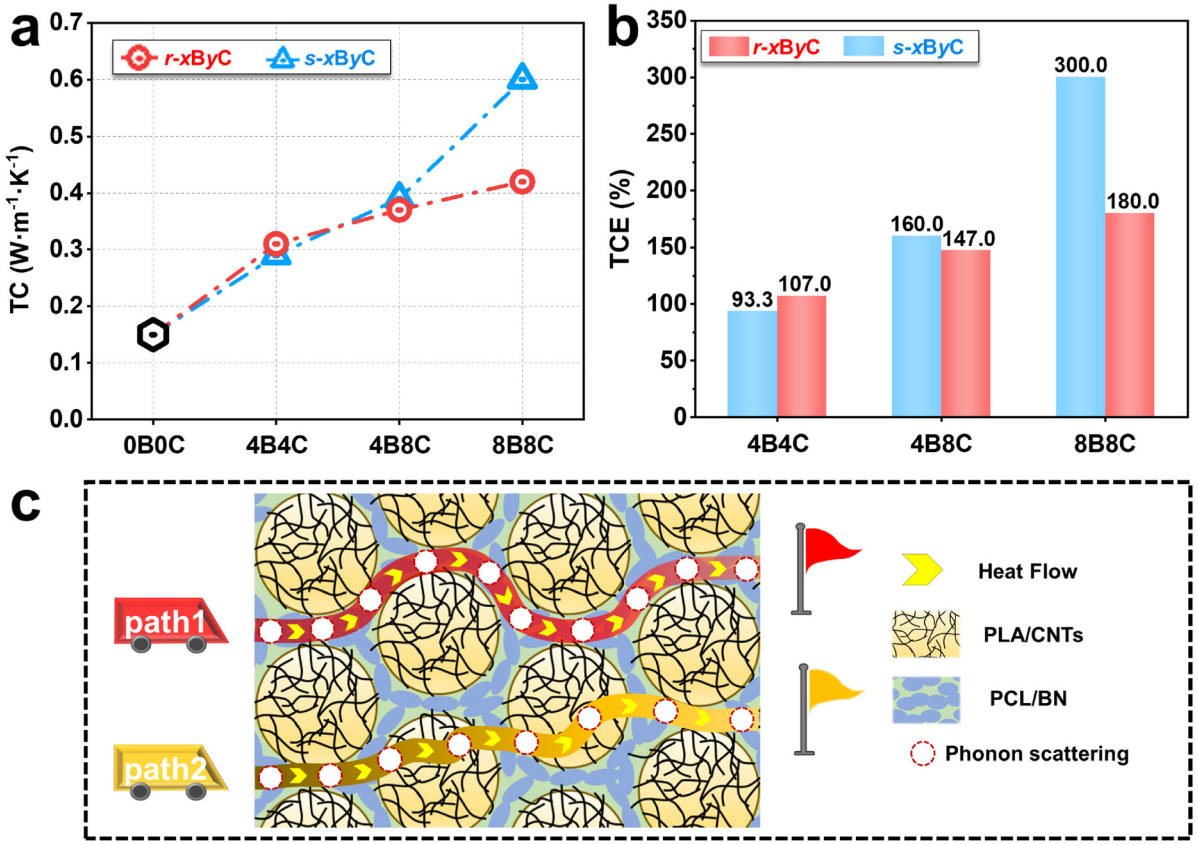

Fig. 6 Thermal conduction properties of various nanocomposites: (a) thermal conductivity (TC); (b) TC enhancement; and (c) schematic diagram of the heat transfer mechanism in segregated structured nanocomposites.

uted to the selective distribution of BN within the PCL matrix of the s-8B8C composite, effectively increasing the BN concentration within the PCL/BN phase to 40 wt%. This selective distribution creates a more robust and stable thermal conduction network, as shown in Fig. 3e$_2$. Additionally, BN in the segregated bands of the s-8B8C composite forms numerous thermal pathways with the CNTs embedded in the PLA microspheres, further improving the heat transfer efficiency. In contrast, in the r-8B8C composite, BN is randomly distributed and fails to establish effective contact between particles. As a result, the TC in r-8B8C is primarily governed by the CNTs, which form less efficient thermal pathways compared to the organized structure of the s-8B8C composite.

Consequently, s-8B8C's TC increased by approximately 300% compared to the PLA/PCL blend, whereas r-8B8C's improvement was about 180%. In summary, the development of "brick–mud" segregated structures within composites plays a crucial role in improving the TC of the polymer matrix, especially when high concentrations of fillers are present in these segregated regions. Fig. 6c demonstrates that in the s-*x*B*y*C composites, heat flow efficiently traverses both through BN within the PCL matrix and along the conductive paths formed by the synergistic interaction of BN and CNTs, significantly enhancing the conduction efficiency. The presence of multiple transmission paths in these composites provides effective solutions to heat accumulation issues. Additionally, the distinct pathways in these composites, comparable to different levels of highways, enable phonons to preferentially select the most unobstructed route.

To assess the thermal efficiency of s-8B8C composites as thermal management materials in electronic devices, both PLA/PCL blends and s-8B8C samples of identical dimensions were subjected to a computer CPU-J1800 heat source. An infrared thermal imager recorded temperature changes on the CPU and composite material surfaces after powering the computer on (0–180s) and off (180–270s), as depicted in Fig. 7. Within 10 s of powering on, the CPU surface temperature rapidly increases. The s-8B8C composite, with its high TC, swiftly transfers heat to its surface, resulting in a rapid temperature rise, whereas the pure PLA/PCL polymer warms up more slowly. Consequently, the s-8B8C surface temperature exceeds that of PLA/PCL at this point. After 10 s, the CPU heating rate and the heating rate of the s-8B8C composite surface both decelerated, indicating the composite's high temperature sensitivity. By around 40 s, the PLA/PCL composite's temperature surpassed that of the s-8B8C and continued to rise. By 180 s, the maximum temperatures of the CPU, PLA/PCL, and s-8B8C reached 38.3 °C, 38.1 °C, and 35.8 °C, respectively. Fig. 7b$_4$ and c$_4$ reveal more severe heat accumulation in the PLA/PCL composite, evident in the CPU's thermal contour, whereas the

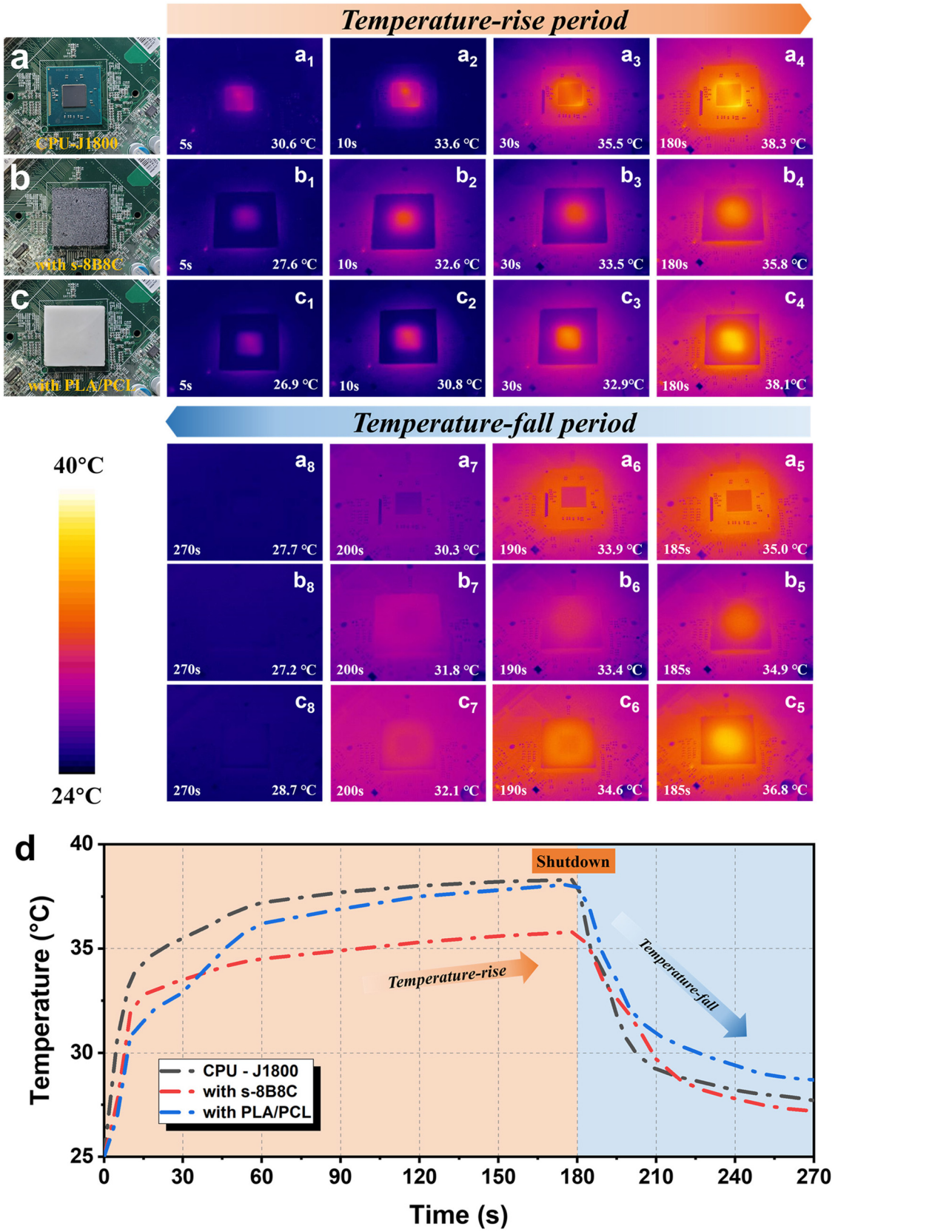

Fig. 7 Computer CPU-J1800 thermal test: (a) CPU-J1800 and its infrared thermogram; (b) s-8B8C and its infrared thermogram as a thermal accessory; (c) PLA/PCL and its infrared thermogram as a thermal accessory; and (d) sample surface temperature profiles during computer start-up (0–180 s) and shutdown (180–270 s).

Table 2 Comparison of the EMI SE, TC and electrical insulation properties of various polymer-based composites

Matrix and filler	Structure	Filler content	TC (W m^{-1} K^{-1})	EMI SE_T (dB, X band)	Electrical insulation	Ref.
PC/EMA/GF/CNT/SF	—	20 wt%	0.804	40.2	No	38
Epoxy/MWCNT/Fe_3O_4@Ag	—	15 wt%	0.46	35	No	39
PVDF/Mxene	—	50 wt%	0.767	34.49	No	40
PP/AlO_3	Segregated	27.5 vol%	1.07	—	Yes	41
Epoxy/BNNS/AgNPs	—	15 vol%	1.01	—	Yes	42
PI/BN	—	30 wt%	0.71	—	Yes	43
NR/BN/CNT	Layered	20 wt%	0.25	22.41	Yes	13
MXene/PDMS/BN	Layered	30 wt%	0.65	35.2	Yes	14
TPU/MWCNTs/BN	Layered	~28 wt%	0.7594	32.27	Yes	44
ER/LMPA/BNNS	Layered	20 vol%	0.22/1.23	20	No	45
		25 vol%	0.34/1.06	14	Yes	
PVDF/MWCNT/BN	Segregated	15 wt%	0.27	10.64	No	46
		45 wt%	0.83	8.68	Yes	
PLA/PCL/CNTs/BN	Segregated	16 wt%	0.6	31.4	Yes	**This work**

s-8B8C composite displayed more uniform heat distribution due to its superior TC. After the computer's operational cycle ends, a temperature differential developed between the CPU, the PLA/PCL composite, and the surrounding environment. This differential is larger than that between the s-8B8C composite and the surrounding environment at 180 s. Between 180 and 270 s, the first two entities show a higher rate of heat dissipation. However, over time, the superior TC of the s-8B8C composite becomes apparent again, ultimately maintaining the lowest temperature at 270s. Additionally, the temperature change of the CPU during this process was recorded, as shown in Fig. S8.† The use of s-8B8C as a cooling accessory results in a lower CPU temperature compared to the other two cases throughout the process. At the start of the 180 second interval, the temperature of the CPU without cooling accessories was 38.3 °C. In comparison, the temperature of the CPU with PLA/PCL cooling accessories peaked at 39.5 °C, while with s-8B8C, it remained at only 36.0 °C. This finding suggests that the distinct "brick–mud" segregated structure of s-8B8C composites significantly enhances their thermal management properties.

Table 2 compares the results of this study with the existing literature on polymer-based composites, covering aspects such as matrix and filler types, composite structure, filler content, TC, EMI SE, and electrical insulating properties. Overall, the s-8B8C composites prepared in this study exhibit clear comprehensive performance advantages at lower filler loadings, including superior electrical insulation compared to electrically and thermally conductive materials, as well as outstanding EMI shielding performance relative to other thermally conductive insulating materials. In contrast to anisotropic multilayer composites that exhibit thermal conductivity, electrical insulation, and EMI shielding, the isotropic properties of the s-8B8C's "brick–mud" segregated structure offer offer greater potential for diverse applications.

Conclusions

Utilizing the differing melting points of PLA and PCL, "brick–mud" segregated (PCL/BN)@(PLA/CNTs) biopolymer nanocomposites were successfully fabricated. Owing to their unique structure, the composites with a low total filler content of 16 wt% (8 wt% each for BN and CNTs) exhibit a total EMI SE of 31.4 dB, a TC of 0.6 W m^{-1} K^{-1}, and a volume resistivity of 7.2×10^{11} Ω cm. The PLA/CNTs composite particles within this structure offer excellent EMI shielding performance, while the continuous PCL/BN phase encapsulates and segregates the conductive PLA/CNTs particles, preventing electron transport between particles and ensuring high volume resistivity. Additionally, numerous thermal conduction pathways formed between BN-BN and BN-CNTs contribute to the composite's enhanced TC. This novel preparation strategy for "brick–mud" segregated composites yields materials with exceptional EMI shielding and thermal conductivity, while maintaining isotropic electrical insulation. Compared to previously reported multilayered composites, which provide insulation only in the shielding direction, this approach offers significant advantages. Although the s-8B8C prototype shows considerable promise as a heat dissipation accessory, further investigation is required to assess its potential as a thermal interface material (TIM). Future studies should focus on a comprehensive evaluation of its flexibility and mechanical properties, alongside optimization of the structural composition, to develop a TIM with enhanced versatility and functionality.

Author contributions

T.L., H.F. and L.D. contributed equally to this work. T.L. and T.K. conceived the concept. H.F., L.D. and C.J. performed investigation and visualization. T.L., H.F. and T.K. analysed and discussed the data. T.L. and H.F. wrote the original draft. T.K., H.V. and M.R.S. reviewed and edited the draft. All authors discussed the results and commented on the manuscript.

Data availability

The data that support the findings of this study are available from the corresponding author, T. R. Kuang, upon reasonable request.

Conflicts of interest

There are no conflicts to declare.

Acknowledgements

The authors gratefully appreciate the financial support provided by the National Natural Science Foundation of China (NOs. 52473050, 52173046 and 51803062) and the Natural Science Foundation of Zhejiang Province (NOs. LZ21E030002 and LQ24E030020).

References

1 M. Wang, X.-H. Tang, J.-H. Cai, H. Wu, J.-B. Shen and S.-Y. Guo, Construction, mechanism and prospective of conductive polymer composites with multiple interfaces for electromagnetic interference shielding: A review, *Carbon*, 2021, **177**, 377–402.

2 T. Liu, H. Feng, C. Jin, M. Pawlak, M. R. Saeb and T. Kuang, Green segregated honeycomb biopolymer composites for electromagnetic interference shielding biomedical devices, *Chem. Eng. J.*, 2024, **493**, 152438.

3 K. Nath, S. Ghosh, S. K. Ghosh, P. Das and N. C. Das, Facile preparation of light–weight biodegradable and electrically conductive polymer based nanocomposites for superior electromagnetic interference shielding effectiveness, *J. Appl. Polym. Sci.*, 2021, **138**(22), 50514.

4 Y. Zhang and J. Gu, A Perspective for Developing Polymer-Based Electromagnetic Interference Shielding Composites, *Nano-Micro Lett.*, 2022, **14**(1), 89.

5 S. Zheng, Y. Wang, Y. Zhu and C. Zheng, Recent advances in structural design of conductive polymer composites for electromagnetic interference shielding, *Polym. Compos.*, 2023, **45**(1), 43–76.

6 R. Chen, Q. He, X. Li, F. Wen, L. Cheng, L. Li, *et al.*, Significant enhancement of thermal conductivity in segregated(GnPs&MWCNTs)@Polybenzoxazine/(Polyether ether ketone) -based composites with excellent electromagnetic shielding, *Chem. Eng. J.*, 2022, **431**, 134049.

7 C. Liang, M. Hamidinejad, L. Ma, Z. Wang and C. B. Park, Lightweight and flexible graphene/SiC-nanowires/poly(vinylidene fluoride) composites for electromagnetic interference shielding and thermal management, *Carbon*, 2020, **156**, 58–66.

8 T. Kuang, H. Guo, W. Guo, W. Liu, W. Li, M. Saeb, M. Vatankhah-Varnosfaderani and S. S. Sheiko, Boosting the Strength and Toughness of Polymer Blends via Ligand-Modulated MOFs, *Adv. Sci.*, 2024, 2407593.

9 B. Wei, L. Zhang and S. Yang, Polymer composites with expanded graphite network with superior thermal conductivity and electromagnetic interference shielding performance, *Chem. Eng. J.*, 2021, **404**, 126437.

10 T. Liu, C. Pei, R. Zeng, J. Zhang, A. Hejna and T. Kuang, Achieving High Thermal Conductivity, Good Electrical Insulation, and Balanced Mechanical Properties in Biodegradable Polymer Composites with Low Filler Content, *ACS Appl. Polym. Mater.*, 2023, **5**(10), 8062–8072.

11 T. Kuang, J. Ju, F. Chen, X. Liu, S. Zhang, T. Liu, *et al.*, Coupled effect of self-assembled nucleating agent, Ni-CNTs and pressure-driven flow on the electrical, electromagnetic interference shielding and thermal conductive properties of poly (lactic acid) composite foams, *Compos. Sci. Technol.*, 2022, **230**, 109736.

12 T. Kuang, J. Zhang, G.-M. Huang, T. Liu and Z.-X. Huang, Multifunctional biopolymer poly (lactic acid)-based triboelectric nanogenerator via controlled construction of secondary electron path, *Nano Energy*, 2024, **128**, 109877.

13 Y. Zhan, E. Lago, C. Santillo, A. E. Del Rio Castillo, S. Hao, G. G. Buonocore, *et al.*, An anisotropic layer-by-layer carbon nanotube/boron nitride/rubber composite and its application in electromagnetic shielding, *Nanoscale*, 2020, **12**(14), 7782–7791.

14 H. Liu, R. Fu, X. Su, B. Wu, H. Wang, Y. Xu, *et al.*, Electrical insulating MXene/PDMS/BN composite with enhanced thermal conductivity for electromagnetic shielding application, *Compos. Commun.*, 2021, **23**, 100593.

15 T. Wang, W.-C. Yu, W.-J. Sun, L.-C. Jia, J.-F. Gao, J.-H. Tang, *et al.*, Healable polyurethane/carbon nanotube composite with segregated structure for efficient electromagnetic interference shielding, *Compos. Sci. Technol.*, 2020, **200**, 108446.

16 W.-C. Yu, J.-Z. Xu, Z.-G. Wang, Y.-F. Huang, H.-M. Yin, L. Xu, *et al.*, Constructing highly oriented segregated structure towards high-strength carbon nanotube/ultrahigh-molecular-weight polyethylene composites for electromagnetic interference shielding, *Composites, Part A*, 2018, **110**, 237–245.

17 P. Zhang, X. Ding, Y. Y. Wang, Y. Gong, K. Zheng, L. Chen, *et al.*, Segregated double network enabled effective electromagnetic shielding composites with extraordinary electrical insulation and thermal conductivity, *Composites, Part A*, 2019, **117**, 56–64.

18 S. K. Srivastava and K. Manna, Recent advancements in the electromagnetic interference shielding performance of nanostructured materials and their nanocomposites: a review, *J. Mater. Chem. A*, 2022, **10**(14), 7431–7496.

19 C.-P. Feng, S.-S. Wan, W.-C. Wu, L. Bai, R.-Y. Bao, Z.-Y. Liu, *et al.*, Electrically insulating, layer structured SiR/GNPs/BN thermal management materials with enhanced thermal conductivity and breakdown voltage, *Compos. Sci. Technol.*, 2018, **167**, 456–462.

20 Y. Yao, X. Zeng, R. Sun, J. B. Xu and C. P. Wong, Highly Thermally Conductive Composite Papers Prepared Based on the Thought of Bioinspired Engineering, *ACS Appl. Mater. Interfaces*, 2016, **8**(24), 15645–15653.

21 L. Guo, S. Ding, S. Yuan, X. Gou, F. Cai, D. Wang, *et al.*, Study on the thermal properties and insulation resistance

of epoxy resin modified by hexagonal boron nitride, *e-Polymers*, 2021, **21**(1), 681–690.

22 L. He, J. Zeng, Y. Huang, X. Yang, D. Li, Y. Chen, *et al.*, Enhanced Thermal Conductivity and Dielectric Properties of h-BN/LDPE Composites, *Materials*, 2020, **13**(21), 4738.

23 Y. Huang, W. Wang, X. Zeng, X. Guo, Y. Zhang, P. Liu, *et al.*, Effects of the filler size on the electrical percolation threshold of carbon black–carbon nanotube–polymer composites, *J. Appl. Polym. Sci.*, 2018, **135**(32), 46517.

24 J.-M. Thomassin, C. Jérôme, T. Pardoen, C. Bailly, I. Huynen and C. Detrembleur, Polymer/carbon based composites as electromagnetic interference (EMI) shielding materials, *Mater. Sci. Eng., R*, 2013, **74**(7), 211–232.

25 Y. Cheng, W. Zhu, X. Lu and C. Wang, One-dimensional metallic, magnetic, and dielectric nanomaterials-based composites for electromagnetic wave interference shielding, *Nano Res.*, 2022, **15**(10), 9595–9613.

26 Q. Liu, Q. Cao, H. Bi, C. Liang, K. Yuan, W. She, *et al.*, CoNi@SiO_2 @TiO_2 and CoNi@Air@TiO_2 Microspheres with Strong Wideband Microwave Absorption, *Adv. Mater.*, 2016, **28**(3), 486–490.

27 Y. Du, Z. Yan, W. You, Q. Men, G. Chen, X. Lv, *et al.*, Balancing MXene Surface Termination and Interlayer Spacing Enables Superior Microwave Absorption, *Adv. Funct. Mater.*, 2023, **33**(34), 2301449.

28 S. Gupta and N.-H. Tai, Carbon materials and their composites for electromagnetic interference shielding effectiveness in X-band, *Carbon*, 2019, **152**, 159–187.

29 Q. Gao, G. Zhang, Y. Zhang, X. Fan, Z. Wang, S. Zhang, *et al.*, Absorption dominated high-performance electromagnetic interference shielding epoxy/functionalized reduced graphene oxide/Ni-chains microcellular foam with asymmetric conductive structure, *Compos. Sci. Technol.*, 2022, **223**, 109419.

30 X. Zhang, J. Tang, Y. Zhong, Y. Feng, X. Wei, M. Li, *et al.*, Asymmetric layered structural design with metal microtube conductive network for absorption-dominated electromagnetic interference shielding, *Colloids Surf., A*, 2022, **643**, 128781.

31 Z. Ali, Y. Gao, B. Tang, X. Wu, Y. Wang, M. Li, *et al.*, Preparation, Properties and Mechanisms of Carbon Fiber/Polymer Composites for Thermal Management Applications, *Polymers*, 2021, **13**(1), 169.

32 Y. Guo, K. Ruan, X. Shi, X. Yang and J. Gu, Factors affecting thermal conductivities of the polymers and polymer composites: A review, *Compos. Sci. Technol.*, 2020, **193**, 108134.

33 C. Huang, X. Qian and R. Yang, Thermal conductivity of polymers and polymer nanocomposites, *Mater. Sci. Eng., R*, 2018, **132**, 1–22.

34 D. R. Salunke and V. Gopalan, Thermal and Electrical behaviors of Boron Nitride/Epoxy reinforced polymer matrix composite—A review, *Polym. Compos.*, 2021, **42**(4), 1659–1669.

35 V. Guerra, C. Wan and T. Mcnally, Thermal conductivity of 2D nano-structured boron nitride (BN) and its composites with polymers, *Prog. Mater. Sci.*, 2019, **100**, 170–186.

36 S. S. Pradhan, L. Unnikrishnan, S. Mohanty and S. K. Nayak, Thermally Conducting Polymer Composites with EMI Shielding: A review, *J. Electron. Mater.*, 2020, **49**(3), 1749–1764.

37 C. Zhan, W. Cui, L. Li, X. Quan, Y. Zhang and F. Xiao, Dual-Aligned carbon nanofiber scaffolds as heat conduction path to enhance thermal conductivity of polymer composites, *Compos. Sci. Technol.*, 2023, **231**, 109823.

38 S. S. Pradhan, L. Unnikrishnan, S. Mohanty, M. Biswal and S. K. Nayak, Thermally conducting hybrid polycarbonate composites with enhanced electromagnetic shielding efficiency, *J. Polym. Res.*, 2021, **28**(12), 463.

39 L. Wang, H. Qiu, C. Liang, P. Song, Y. Han, Y. Han, *et al.*, Electromagnetic interference shielding MWCNT-Fe_3O_4@Ag/epoxy nanocomposites with satisfactory thermal conductivity and high thermal stability, *Carbon*, 2019, **141**, 506–514.

40 K. Rajavel, S. Luo, Y. Wan, X. Yu, Y. Hu, P. Zhu, *et al.*, 2D $Ti_3C_2T_x$ MXene/polyvinylidene fluoride (PVDF) nanocomposites for attenuation of electromagnetic radiation with excellent heat dissipation, *Composites, Part A*, 2020, **129**, 105693.

41 X. Zhang, X. Xia, H. You, T. Wada, P. Chammingkwan, A. Thakur, *et al.*, Design of continuous segregated polypropylene/Al_2O_3 nanocomposites and impact of controlled Al_2O_3 distribution on thermal conductivity, *Composites, Part A*, 2020, **131**, 105825.

42 Y. Wu, X. Zhang, A. Negi, J. He, G. Hu, S. Tian, *et al.*, Synergistic Effects of Boron Nitride (BN) Nanosheets and Silver (Ag) Nanoparticles on Thermal Conductivity and Electrical Properties of Epoxy Nanocomposites, *Polymers*, 2020, **12**(2), 426.

43 Y. Guo, Z. Lyu, X. Yang, Y. Lu, K. Ruan, Y. Wu, *et al.*, Enhanced thermal conductivities and decreased thermal resistances of functionalized boron nitride/polyimide composites, *Composites, Part B*, 2019, **164**, 732–739.

44 G. Wang, X. Liao, F. Zou, P. Song, W. Tang, J. Yang, *et al.*, Flexible TPU/MWCNTs/BN composites for frequency-selective electromagnetic shielding and enhanced thermal conductivity, *Compos. Commun.*, 2021, **28**, 100953.

45 P. Zhang, R. Tian, X. Zhang, X. Ding, Y. Wang, C. Xiao, *et al.*, Electromagnetic interference shielding epoxy composites with satisfactory thermal conductivity and electrical insulation performance enabled by low-melting-point alloy layered structure, *Composites, Part B*, 2022, **232**, 109611.

46 P. Zhang, X. Ding, Y. Wang, Y. Gong, K. Zheng, L. Chen, *et al.*, Segregated double network enabled effective electromagnetic shielding composites with extraordinary electrical insulation and thermal conductivity, *Composites, Part A*, 2019, **117**, 56–64.

